

Aortic Valve Disease Detection from PPG via Physiology-Informed Self-Supervised Learning

Jiaze Wang^{1,5,†}, Qinghao Zhao^{2,†}, Zizheng Chen^{1,†}, Zhejun Sun¹, Deyun Zhang³, Yuxi Zhou^{1,4,*}, and Shenda Hong^{5,6,7,8,*}

¹Department of Computer Science, Tianjin University of Technology, Tianjin, China

²Department of Cardiology, Peking University People's Hospital, Beijing, China

³HeartVoice Medical Technology, Hefei, China

⁴DCST, BNRist, RIIT, Institute of Internet Industry, Tsinghua University, Beijing, China

⁵National Institute of Health Data Science, Peking University, Beijing, China

⁶Institute of Medical Technology, Peking University Health Science Center, Beijing, China

⁷Institute for Artificial Intelligence, Peking University, Beijing, China

⁸State Key Laboratory of Vascular Homeostasis and Remodeling, NHC Key Laboratory of Cardiovascular Molecular Biology and Regulatory Peptides, Peking University, Beijing, China

[†]These authors contributed equally

^{*}Correspondence: joy_yuxi@pku.edu.cn, hongshenda@pku.edu.cn

ABSTRACT

Background: Traditional diagnosis of aortic valve disease relies on echocardiography, but its cost and required expertise limit its use in large-scale early screening. Photoplethysmography (PPG) has emerged as a promising screening tool due to its prevalence in wearable devices and its ability to reflect hemodynamic dynamics. However, the extreme scarcity of gold-standard labeled PPG data needed for building accurate models severely constrains the effectiveness of data-driven methods.

Objective: To address this challenge, this study proposes and validates a new paradigm, Physiology-Guided Self-Supervised Learning (PG-SSL), aimed at unlocking the value of large-scale unlabeled PPG data for efficient screening of Aortic Stenosis (AS) and Aortic Regurgitation (AR).

Methods: We utilized a large-scale cohort from the UK Biobank, comprising over 170,000 unlabeled PPG samples. Our PG-SSL framework first formalizes clinical knowledge into a set of PPG morphological phenotypes. A pulse pattern recognition proxy task is then constructed and executed on this large cohort for self-supervised pre-training. Subsequently, we designed a dual-branch, gated-fusion architecture to efficiently fine-tune the pre-trained model on a small, labeled subset.

Results: The proposed PG-SSL framework achieved an Area Under the Curve (AUC) of 0.765 and 0.776 for the AS and AR screening tasks, respectively. Compared to a supervised learning baseline trained directly on limited labeled data, our method demonstrated a significant performance improvement. Furthermore, multivariable analysis validated the model output as an independent digital biomarker, retaining significant prognostic value after adjusting for standard clinical risk factors.

Conclusion: This study demonstrates that PG-SSL is a powerful paradigm for effectively unlocking the value of unlabeled physiological signal data. This method provides a novel, domain knowledge-driven pathway for addressing the pervasive issue of label scarcity in medical artificial intelligence and shows great potential for developing low-cost, large-scale AVD early screening tools.

KEYWORDS

Aortic Valve Disease, Photoplethysmography (PPG), Physiology-Guided Self-Supervised Learning, Few-Shot Learning, Disease Screening, UK Biobank

INTRODUCTION

Valvular heart disease (VHD) stands as a primary cause of global cardiovascular morbidity and mortality, with its burden escalating dramatically alongside the aging of the world's population¹. Among all forms of VHD, aortic valve disease (AVD), which predominantly includes aortic stenosis (AS) and aortic regurgitation (AR), represents the most life-threatening category, accounting for a staggering 61% of all VHD-related deaths². However, a stark clinical reality persists: despite the severe consequences of AVD, its early diagnosis is exceptionally challenging. The disease progression is typically insidious, with patients remaining largely asymptomatic until the optimal window for intervention has passed. Once symptoms emerge, the average life expectancy can plummet to as little as two to three years, this widespread diagnostic delay is fundamentally rooted in the failure of traditional screening methods³. Therefore, this study aims to develop a scalable, low-cost screening technology capable of identifying high-risk individuals during the asymptomatic phase of AVD, with the goal of fundamentally transforming the current reactive paradigm of diagnosis and treatment.

From the clinical gold standard to emerging portable sensors, existing solutions face fundamental bottlenecks in meeting the requirements of convenience, reliability, and informational directness necessary for large-scale screening. While imaging-based gold standards like transthoracic echocardiography (TTE) offer diagnostic precision⁴, their heavy reliance on specialized personnel and dedicated facilities makes them impractical for widespread deployment³. Emerging portable technologies based on chest wall vibrations, such as digital phonocardiography (PCG), seismocardiography (SCG), and gyrocardiography (GCG)⁵⁻⁷, have a critical vulnerability: their performance is highly dependent on stable and precise physical contact with the skin, making it difficult for non-expert users to ensure data quality and reproducibility. The more widely used portable electrocardiogram (ECG)^{8,9}, in turn, faces a fundamental limitation of informational indirectness. AVD is inherently a mechanical disorder, whereas the ECG captures electrical activity that is merely an indirect, delayed, and non-specific consequence of long-term hemodynamic stress. This renders it insensitive to early-stage disease. In summary, existing portable solutions are either unreliable due to their physical dependencies or insensitive due to their informational indirectness, leaving a clear technological void for a novel sensing modality that is both easily deployable and directly reflective of hemodynamic dynamics.

To address these challenges, there is an urgent need for a sensing technology that can directly and reliably capture hemodynamic dynamics while being amenable to large-scale deployment. Photoplethysmography (PPG) presents a highly compelling solution. As an optical sensing technology already integrated into hundreds of millions of consumer wearable devices worldwide, PPG possesses an unparalleled hardware foundation to become a ubiquitous screening tool¹⁰. More critically, the core advantage of PPG lies in its informational directness. By measuring pulsatile blood volume changes in peripheral tissues, it effectively captures the morphology of the central arterial pressure wave^{11,12}, offering a unique, non-invasive window into the hemodynamic disturbances caused by valvular dysfunction. Specifically, the obstructed ejection in AS or the abnormal diastolic pressure dynamics in AR are expected to leave discernible signatures on the contour, amplitude, and timing features of the PPG waveform. Indeed, the feasibility of using PPG morphological analysis to assess complex cardiovascular states, such as blood pressure, arterial stiffness, and even atrial fibrillation, has been extensively validated^{13,14}.

While nascent studies have explored the use of PPG for detecting isolated AS^{15,16}, its application to AR screening remains a largely uncharted frontier. Crucially, a unified AI framework capable of simultaneously screening for and differentiating between AS, AR, and healthy states is non-existent. Therefore, given its immense technological potential and the current void in its application, PPG offers an unprecedented opportunity to build the next generation of early AVD screening paradigms.

Despite the unique physiological perspective PPG offers for AVD screening, translating this potential into accurate and robust algorithms faces a dual challenge, spanning from feature representation to data availability. First, the PPG waveform alterations caused by valvular dysfunction are often relatively subtle and are frequently confounded by morphological variations arising from individual physiological differences such as age and arterial stiffness¹². This inherent signal complexity demands models with a strong capacity for signal decoupling to isolate weak pathological signatures from a noisy physiological background¹⁴. This feature extraction dilemma is, in turn, dramatically amplified by the scarcity of high-quality supervised data. In existing public datasets and large cohort studies, the number of high-quality PPG samples that are rigorously aligned with gold-standard diagnostic labels for AS/AR (such as those from echocardiography) is generally limited. This scarcity of labeled data, a widely recognized bottleneck in the field of medical artificial intelligence¹⁷, severely constrains the effective training of complex deep learning models. Consequently, the field confronts a central paradox: the need for powerful models to learn highly similar features starkly contrasts with the lack of large-scale, high-quality labeled data required to train them. This paradox compels a move beyond traditional supervised learning frameworks to explore new paradigms.

To break the core paradox defined by the dual challenges of intricate feature extraction and label scarcity, we introduce a novel framework based on Physiology-Guided Self-Supervised Learning (PG-SSL). The central idea of PG-SSL is to bypass the reliance on direct pathological labels. Instead, it leverages large-scale, unlabeled PPG data to distill latent knowledge through a carefully designed, physiology-guided pretext task¹⁸. Specifically, we formalize established clinical physiological knowledge of AVD—such as the *pulsus parvus et tardus* pattern reflecting obstructed ejection in AS, and the *water-hammer pulse* pattern indicating diastolic regurgitation in AR¹⁹—into a set of computable PPG morphological phenotypes. Crucially, these phenotypes serve as pseudo-labels to construct a proxy classification task on a massive dataset of over 170,000 unlabeled samples. The sheer scale of this dataset provides statistical robustness to the inherently noisy proxy task, compelling the model to learn beyond the ambiguities of individual samples and capture the more fundamental, generalizable features that differentiate underlying hemodynamic patterns. This pre-training process effectively transforms the unlabeled data into a rich latent knowledge base for AVD screening. Building on this foundation, the PG-SSL framework then requires only a minimal amount of labeled AS/AR data for fine-tuning, efficiently adapting the universal hemodynamic knowledge encoded in the pre-trained model to the downstream AVD classification tasks. Our validation on a large-scale cohort dataset demonstrates that, compared to a supervised baseline trained directly on limited labels, the PG-SSL pre-trained model significantly improves the screening performance for AS and AR. This result strongly validates that our PG-SSL paradigm can effectively mitigate the dual challenges of label scarcity and feature confounding, offering a novel, domain knowledge-driven pathway for data-limited medical signal analysis.

RESULTS

Dataset and Cohort Definition

The data for this study were derived from the UK Biobank, a large-scale biomedical database containing genetic and health information from over 500,000 individuals. Photoplethysmography (PPG) data were extracted from Field 4205, collected using the PulseTrace PCA2 device. The device outputs an averaged waveform calculated from a 10-to-15-second recording, standardized to 100 sampling points. For participants with multiple longitudinal records, this study selected only the baseline acquisition data. Consequently, the data format consists of a single-beat waveform corresponding to a single patient. We utilized these raw signals directly without performing additional preprocessing.

The experiment constructed two independent data cohorts. First, data from 170,702 participants not labeled with aortic valve disease in the library were utilized as the unlabeled pre-training set. Second, a labeled dataset was constructed for downstream fine-tuning. Positive cases were identified based on ICD-10 diagnostic codes (AS: I35.0/I06.0; AR: I35.1/I06.1) and self-reported medical history (Code 20002). Considering the insidious onset and progressive hemodynamic nature of AVD, the definition of positive cases was extended to include diagnoses confirmed within one year following PPG acquisition, thereby capturing undiagnosed prevalent cases in the latent phase. Patients with a history of aortic valve intervention were excluded based on OPCS-4 procedural codes (K26, K30, K35.2). Ultimately, 5,460 subjects were included, comprising 245 AS patients and 213 AR patients, of which 81 were identified as Mixed Aortic Valve Disease (Mixed AVD). The dataset was partitioned by subject into training (64%), validation (16%), and test (20%) sets. Regarding baseline characteristics (Table 1), continuous variables are summarized as mean \pm standard deviation, while categorical variables are reported as counts and percentages.

Table 1: Baseline characteristics of study cohorts. Continuous variables are mean \pm SD; categorical are n (%). P-values compare AS/AR vs Control. AS: aortic stenosis; AR: aortic regurgitation.

Characteristic	Pre-train (N=170,702)	Total (N=5,460)	AS (N=245)	AR (N=213)	Control (N=5,083)	<i>P</i> _{AS}	<i>P</i> _{AR}
Age (years)	56.77 \pm 8.16	56.87 \pm 8.09	62.00 \pm 6.17	60.36 \pm 7.09	56.55 \pm 8.10	<0.001	<0.001
Sex							
Male	78,249 (45.8%)	2,530 (46.3%)	151 (61.6%)	125 (58.7%)	2,308 (45.4%)	<0.001	<0.001
Race							
White	154,661 (90.6%)	4,955 (90.8%)	229 (93.5%)	194 (91.1%)	4,609 (90.7%)	0.172	0.937
Asian	6,112 (3.6%)	191 (3.5%)	7 (2.9%)	8 (3.8%)	177 (3.5%)	0.731	0.982
Black	4,598 (2.7%)	132 (2.4%)	3 (1.2%)	4 (1.9%)	126 (2.5%)	0.286	0.820
BMI (kg/m ²)	27.46 \pm 4.83	27.58 \pm 4.89	29.79 \pm 5.61	28.31 \pm 4.84	27.47 \pm 4.83	<0.001	0.015
Systolic BP (mmHg)	137.82 \pm 18.62	138.39 \pm 19.10	142.51 \pm 19.08	141.83 \pm 21.21	138.10 \pm 18.99	<0.001	0.012
Diastolic BP (mmHg)	82.13 \pm 10.07	82.12 \pm 10.33	78.20 \pm 10.80	78.19 \pm 11.36	82.39 \pm 10.22	<0.001	<0.001
Heart Rate (bpm)	68.64 \pm 11.16	68.36 \pm 11.32	67.28 \pm 12.44	67.61 \pm 11.57	68.42 \pm 11.24	0.164	0.317
Arterial Stiffness (m/s)	9.34 \pm 4.05	9.32 \pm 5.20	10.00 \pm 3.10	9.53 \pm 3.17	9.29 \pm 5.32	<0.001	0.294
Reflection Index (%)	67.73 \pm 32.19	67.96 \pm 30.75	66.84 \pm 18.30	66.76 \pm 14.50	68.07 \pm 31.53	0.328	0.230
HbA1c (mmol/mol)	36.32 \pm 6.89	36.35 \pm 6.78	39.25 \pm 10.01	37.65 \pm 8.84	36.19 \pm 6.54	<0.001	0.023
Cholesterol (mmol/L)	5.68 \pm 1.15	5.64 \pm 1.15	5.19 \pm 1.24	5.24 \pm 1.17	5.67 \pm 1.14	<0.001	<0.001
Current Smoker	17,225 (10.2%)	544 (10.0%)	21 (8.6%)	21 (10.0%)	510 (10.1%)	0.514	1.000
Daily Alcohol Intake	34,363 (20.2%)	1,130 (20.8%)	58 (23.8%)	39 (18.6%)	1,050 (20.7%)	0.284	0.508
Hypertension	64,978 (38.1%)	2,182 (40.0%)	197 (80.4%)	157 (73.7%)	1,895 (37.3%)	<0.001	<0.001
Diabetes Mellitus	16,582 (9.7%)	566 (10.4%)	63 (25.7%)	35 (16.4%)	486 (9.6%)	<0.001	0.001
Hyperlipidemia	40,177 (23.5%)	1,368 (25.1%)	172 (70.2%)	116 (54.5%)	1,138 (22.4%)	<0.001	<0.001
Chronic Kidney Disease	6,470 (3.8%)	243 (4.5%)	49 (20.0%)	37 (17.4%)	178 (3.5%)	<0.001	<0.001
CAD / MI	19,747 (11.6%)	779 (14.3%)	158 (64.5%)	110 (51.6%)	564 (11.1%)	<0.001	<0.001
Atrial Fibrillation	12,131 (7.1%)	488 (8.9%)	106 (43.3%)	92 (43.2%)	330 (6.5%)	<0.001	<0.001
Stroke	5,694 (3.3%)	207 (3.8%)	41 (16.7%)	32 (15.0%)	151 (3.0%)	<0.001	<0.001

Screening Performance and Pre-training Paradigms

We comprehensively evaluated the screening performance of the PiLA framework on the independent test set. As shown in Table 2, PiLA demonstrated superior performance in both tasks, achieving an Area Under the Curve (AUC) of 0.7645 for AS and 0.7756 for AR. The Receiver Operating Characteristic (ROC) curves for both tasks are illustrated in Figure 1 (A, B). For clinical screening, beyond global discrimination, the detection capability at specific operating points is critical. Notably, at a specificity of 60% (S@60Sp), PiLA identified 77.6% of AS patients and 78.6% of AR patients. This result significantly outperforms supervised learning baselines such as ResNet1D-18, indicating that PiLA effectively stratifies the vast majority of potential patients into the moderate-to-high risk zone, thereby minimizing missed diagnoses and demonstrating strong capability for early risk capture.

Beyond discrimination capability, the reliability of model predicted probabilities is equally critical for clinical decision-making. As shown in the calibration curves (Figure 1C), PiLA’s predicted probabilities closely align with the true prevalence along the diagonal. Notably, within the [0, 0.45] risk interval, which is the primary focus for general population screening, the model exhibited no significant overconfidence or underestimation of risk. To further assess the practical utility of the model in resource-constrained scenarios, we calculated the screening enrichment factor (Figure 1D), incorporating a Savitzky-Golay filter to ensure statistical robustness. The analysis revealed a significant early enrichment effect: for AS, the enrichment factor peaked at 4.68x within the top 5% of the population with the highest risk scores; for AR, the model maintained an improvement of over 3.45x within the top 10% interval. This implies that confirming diagnoses only for the top 5-10% of individuals flagged as high-risk by PiLA would yield a detection efficiency 3 to 5 times higher than random screening, thereby substantially improving the cost-effectiveness of large-scale screening.

To verify the impact of model architecture, we compared PiLA with two advanced time-series models: (1) TimesNet²⁰, a general-purpose model capturing complex periodicities via temporal 2D variation modeling; and (2) Attn-LRCN²¹, a state-of-the-art (SOTA) model in PPG affect recognition combining LSTM with attention mechanisms to extract long-range dependencies. Despite their success in their respective domains, neither model surpassed PiLA in terms of AUC in this study. Specifically, TimesNet achieved an AUC of only 0.6793 on the AR task, notably lower than PiLA’s 0.7756; while Attn-LRCN showed reasonable sensitivity, its overall discriminative power did not exceed the proposed framework. This performance bottleneck suggests that under constraints of *small-sample* sizes and *single-beat* signals, blindly increasing model complexity leads to overfitting, whereas PiLA effectively mitigates this issue by introducing physiological priors.

This bottleneck further suggests that relying solely on limited labeled data, simply increasing model complexity cannot overcome overfitting. To unlock the potential of large-scale unlabeled data, we subsequently evaluated generic self-supervised learning (Generic SSL) paradigms, which have been widely explored for addressing medical data scarcity^{17,22,23}. Representative approaches include contrastive learning (e.g., SimCLR)²⁴ and signal reconstruction tasks^{25,26}. Experimental results show that these generic paradigms did not yield the expected performance gains. Specifically, for SimCLR, we implemented a standard augmentation pipeline containing random crop with padding, Gaussian jitter, and magnitude scaling. Results indicated that the random perturbations introduced by SimCLR, while increasing sample diversity, likely disrupted the fine-grained waveform morphological invariance relied upon for AS diagnosis (e.g., Gaussian jitter masking subtle notches, magnitude scaling altering pulse pressure features). Reconstruction tasks tended to restore global contours rather than capturing subtle pathological details. Similarly, direct K-Means clustering on raw data, while capturing statistical regularities, lacked pathological directionality and was prone to being dominated by high-variance non-pathological

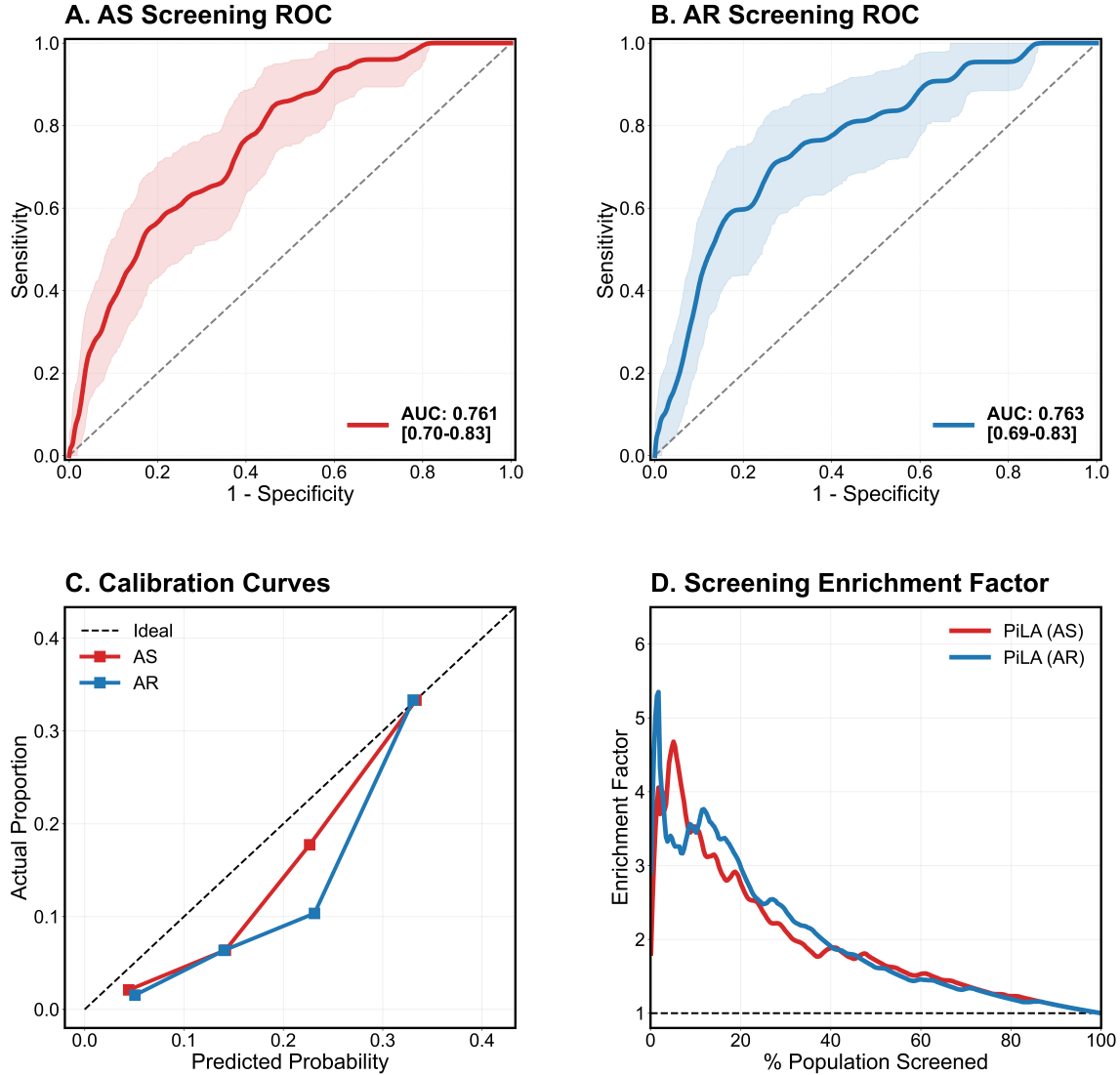


Figure 1: Performance evaluation of the model on the independent test set. (A, B) ROC curves for AS and AR detection. The model achieves an AUC of 0.765 for AS and 0.776 for AR. (C) Calibration curves. The axes focus on the $[0, 0.45]$ interval, showing high consistency between predicted probabilities and observed prevalence. (D) Screening enrichment factor (Lift curve). The curves, smoothed using a Savitzky-Golay filter, demonstrate significant disease prevalence enrichment in the top 5%-10% high-risk population (peaking at 4.68x for AS), verifying the utility of the model for optimizing medical resource allocation.

features (e.g., heart rate variations). These findings collectively reveal the limitation of Generic SSL in processing precise physiological signals: its “physiology-agnostic” nature makes it difficult to effectively capture the subtle pathological fingerprints associated with valvular diseases.

Table 2: Comparison of Screening Performance for Aortic Stenosis and Regurgitation. The table presents the Area Under the Receiver Operating Characteristic Curve (AUROC), Sensitivity at 60% Specificity (S@60Sp), and Balanced Accuracy (BalAcc). The table is stratified by task: Panel A for Aortic Stenosis (AS) and Panel B for Aortic Regurgitation (AR).

Method	AUROC	S@60Sp	BalAcc
<i>Panel A: Aortic Stenosis (AS)</i>			
<i>Supervised Baselines</i>			
ResNet1D (Baseline)	0.6985	0.6531	0.6613
TimesNet ²⁰	0.6977	0.7347	0.6821
Attn-LRCN ²¹	0.7020	0.7551	0.7041
<i>Self-Supervised Paradigms</i>			
SimCLR ²⁴	0.7175	0.6939	0.6939
Reconstruction ²⁶	0.7216	0.7143	0.6922
K-Means	0.7000	0.6735	0.6576
Feature-based Clustering	0.7201	0.6735	0.6613
PiLA (Ours)	0.7645	0.7755	0.7072
<i>Panel B: Aortic Regurgitation (AR)</i>			
<i>Supervised Baselines</i>			
ResNet1D (Baseline)	0.7013	0.7143	0.6786
TimesNet ²⁰	0.6793	0.6486	0.6494
Attn-LRCN ²¹	0.7236	0.7297	0.7025
<i>Self-Supervised Paradigms</i>			
SimCLR ²⁴	0.7252	0.6905	0.6819
Reconstruction ²⁶	0.7508	0.7619	0.7033
K-Means	0.7199	0.7619	0.7029
Feature-based Clustering	0.6783	0.6786	0.6289
PiLA (Ours)	0.7756	0.7857	0.7490

Given the limitations of generic methods, physiology-guided approaches emerge as a promising direction. Indeed, integrating domain knowledge into learning—known as knowledge-guided machine learning (KGML)—has become critical for advancing AI in complex scientific domains²⁷. While Physics-Informed Neural Networks (PINNs) have succeeded by embedding physical laws²⁸, they rely on precise mathematical equations, making them less adaptable to the complex biological variability of AVD; consequently, a more flexible strategy involves guiding models using signal-level feature points or explicit rules, as explored in recent studies^{29–31}. Drawing inspiration from this idea, we constructed a Feature-based Clustering pre-training strategy as a validation baseline, utilizing six key pulse wave metrics provided by the UK Biobank (including pulse rate, reflection index, etc.) to generate pseudo-labels. However, results showed that this strategy even caused significant negative transfer on the AR task (AUC dropped to 0.6783). This result indicates that, in our experimental setting, relying solely on low-dimensional scalar features is insufficient to construct effective pathological representations, as they lose the high-dimensional morphological details that deep neural networks can capture. In contrast, PiLA transforms clini-

cal diagnostic logic (Tardus/WHP rules³²) into a proxy task; this strategy acts as a potent “pathological filter,” forcing the model to learn deep morphological patterns consistent with specific clinical definitions from massive data, thereby achieving optimal performance on both tasks.

Physiological Fidelity and Robustness Analysis

Visualizing Physiological Basis

To elucidate the decision-making logic of the PiLA system and verify its physiological consistency, we visualized the activation heatmaps of the feature extractor’s terminal layer (adapt_conv) using 1D Grad-CAM techniques. As shown in Figure 2, the model did not rely on background noise but instead formed highly specific attention patterns for different pathological categories, which align closely with established clinical hemodynamic mechanisms.

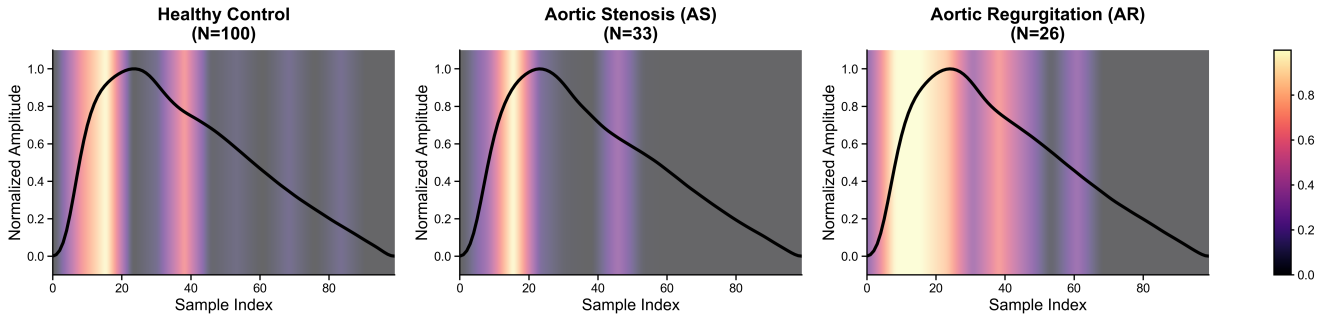


Figure 2: Grad-CAM visualization of model attention across different groups. (Left) Healthy controls show diffuse attention, verifying holistic waveform integrity. (Center) AS patients show focused attention on the delayed systolic upstroke and dicrotic notch. (Right) AR patients exhibit broad coverage over the high-amplitude systolic phase and early diastolic collapse, reflecting volume overload.

In the Aortic Stenosis (AS) group, the model exhibited a highly focused attention pattern, primarily targeting the *systolic upstroke* and showing secondary attention at the *dicrotic notch* on the descent. The highlighting of the upstroke corresponds to the classic *Pulsus Parvus* feature of AS, characterized by a delayed pressure rise due to left ventricular outflow obstruction³³. Notably, our cohort is predominantly elderly, where arterial stiffness typically increases pulse wave velocity and steepens the upstroke, potentially causing a “pseudo-normalization” phenomenon that masks pathological features³⁴. However, the model precisely locked onto this region, suggesting that by leveraging multi-modal derivative inputs (VPG/APG), it successfully extracted microscopic acceleration anomalies hidden within the stiffened background, effectively de-confounding the signal. Furthermore, the secondary attention on the descent reflects the model’s capture of *Prolonged Ejection Time*. As ejection resistance increases, aortic valve closure is delayed³³, and the model aids diagnosis by localizing the temporal shift of the dicrotic notch, thereby constructing a dual verification logic of “morphological features” and “temporal features.”

In sharp contrast to the point-like focus in AS, the Aortic Regurgitation (AR) group’s heatmaps displayed a significant “*Broad Coverage*” feature, spanning 0-60% of the cardiac cycle, with a focus on the entire ascent and the initial notch region of the descent. This broad attention reflects the volume overload mechanism of AR. Diastolic regurgitation leads to a significant increase in left ventricular stroke volume, inducing a *Hyperdynamic State* in the vascular wall throughout systole³⁵. Since PPG signals inherently reflect blood volume changes in the microvascular bed,

the model directly responds to this high-dynamic expansion by attending to the broad high-amplitude envelope. Simultaneously, the strong attention at the initial descent corresponds to the blurring or disappearance of the dicrotic notch (*Slurred Incisura*). Due to valvular incompetence, diastolic pressure cannot be maintained, resulting in a typical *Rapid Run-off* phenomenon³⁶. The model acutely captured this key morphological absence as a core basis for identifying AR.

The Healthy Control group showed the most diffuse attention distribution, without the extreme focal points seen in the pathological groups. This reveals that the model employs a decision logic of “*Holistic Integrity Verification*.” Rather than searching for a specific pathological fingerprint, the model scans the entire cardiac cycle in healthy samples: verifying the steepness of the upstroke to rule out AS, and confirming the clarity of the dicrotic notch to rule out AR. This judgment logic, based on the overall *Normality* of the waveform, aligns with standard photoplethysmogram morphological definitions³⁷, demonstrating the model’s robust specificity.

Completeness of Deep Features

To investigate whether explicit physiological priors could further enhance the model’s discriminative power, we designed a rigorous late fusion experiment. We extracted 22-dimensional classic PPG morphological features, covering time intervals, waveform slopes, and advanced amplitude statistics (e.g., T_1 , $Slope_1$, KR_1 ; see Appendix for details), and implemented a strict leakage-proof standardization strategy.

Experimental results showed that introducing these handcrafted features actually led to a slight performance degradation. The AUROC of the fused model dropped to 0.7415 for the AS task and 0.7514 for the AR task, both lower than the baseline performance of the PiLA pure deep feature model. This phenomenon strongly confirms the high completeness of the deep features extracted by PiLA. Through multi-modal self-supervised learning, the model has internalized all discriminative morphological information; handcrafted features are merely a redundant subset of the deep feature space, and forced fusion introduced additional noise.

The deeper reason lies in the limitations of handcrafted features in dealing with complex confounding factors. Research by Hungerford et al. indicates that waveform changes caused by vascular aging overlap significantly with the pathological features of AS³⁴. Handcrafted features are inherently linear and low-dimensional, unable to effectively decouple “AS-induced waveform changes” from “background noise caused by vascular aging.” In contrast, PiLA’s deep features, through non-linear mapping, successfully captured high-order dynamic patterns hidden in the derivative space, thereby significantly outperforming traditional feature engineering in anti-interference capability.

Early Detection and Long-term Prognostic Value

Temporal Sensitivity and Disease Progression Trajectories

To evaluate the model’s early warning capabilities, we stratified the positive cohort based on the time interval from PPG acquisition to clinical diagnosis (Time-to-Event). The quantitative results are presented in Figure 3 and Table 3. The analysis reveals distinct progression trajectories for AS and AR, reflecting their divergent hemodynamic mechanisms.

For Aortic Stenosis (AS), the model exhibited a significant dose-response relationship with time. The AUROC steadily increased from 0.616 in the remote group (> 10 years) to 0.721 in the proximate group (1 – 3 years) (Figure 3C). This continuous performance improvement aligns closely with the natural history of AS: as leaflet calcification accumulates and the orifice area linearly narrows, left ventricular outflow obstruction worsens, making the “*Pulsus Tardus*” feature in the PPG waveform increasingly prominent and thus more accurately captured by the model.

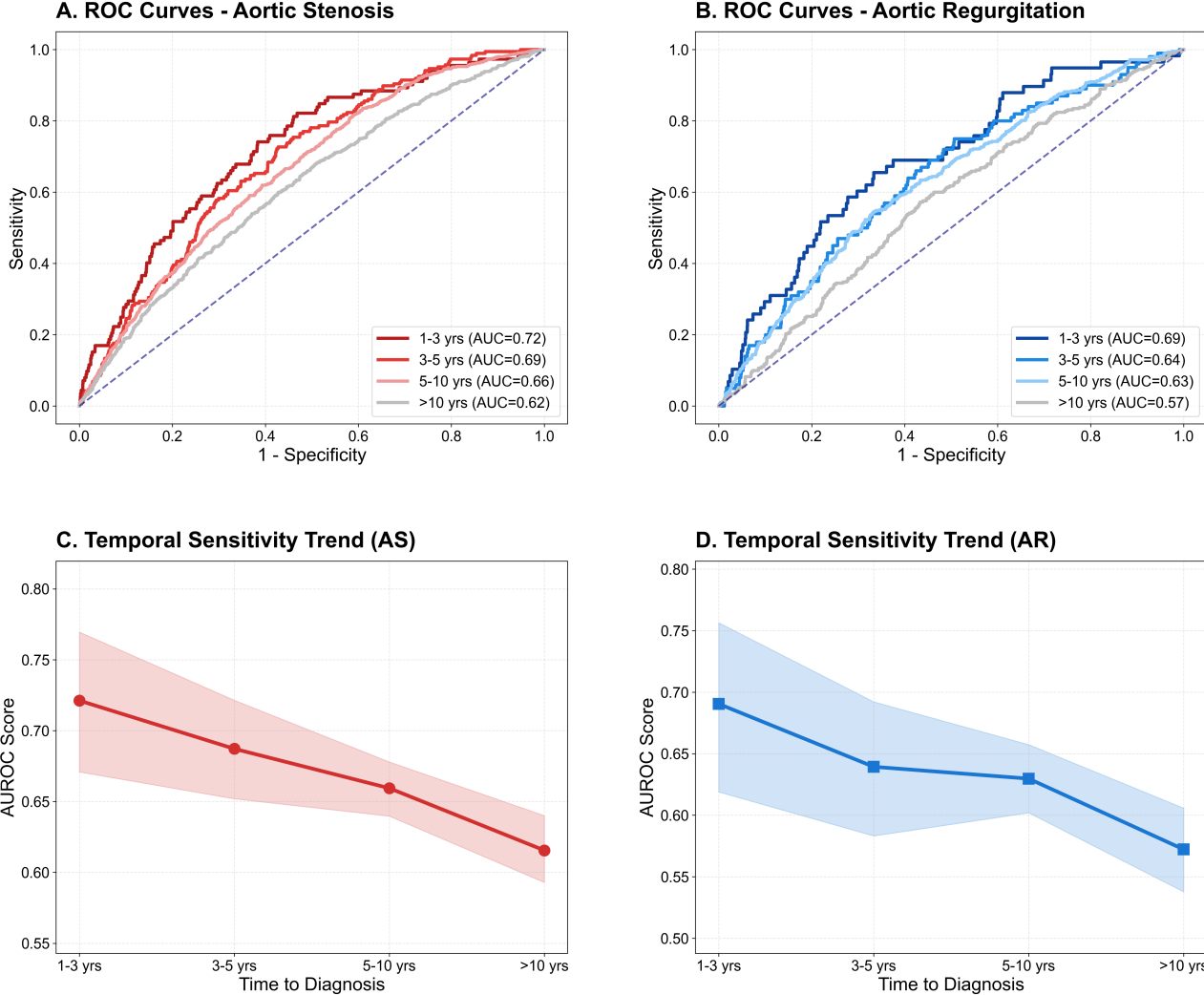


Figure 3: Temporal sensitivity analysis of the model. (A, B) ROC curves stratified by time-to-diagnosis intervals for AS and AR. (C, D) Trends of AUROC scores over time. The shaded areas represent 95% confidence intervals. AS shows a linear progression trend, while AR exhibits a plateau phase corresponding to physiological compensation.

Table 3: Model Performance Stratified by Time-to-Diagnosis Intervals

Disease	Time Interval	AUROC (95% CI)	Sens @ 80% Spec
Aortic Stenosis (AS)	1-3 Years	0.721 (0.671 – 0.770)	49.1%
	3-5 Years	0.687 (0.652 – 0.721)	38.5%
	5-10 Years	0.659 (0.640 – 0.678)	37.2%
	>10 Years	0.616 (0.593 – 0.640)	33.2%
Aortic Regurgitation (AR)	1-3 Years	0.691 (0.619 – 0.756)	44.8%
	3-5 Years	0.639 (0.583 – 0.692)	34.0%
	5-10 Years	0.630 (0.602 – 0.657)	34.0%
	>10 Years	0.572 (0.538 – 0.606)	25.2%

In contrast, Aortic Regurgitation (AR) displayed a unique non-linear evolution pattern (Figure 3D). Although the proximate group (AUC 0.691) significantly outperformed the remote groups, a clear performance *plateau* (AUC \approx 0.630–0.640) was observed between the intermediate (3–5 years) and remote (5–10 years) phases. Physiologically, this corresponds to the long *Compensated Phase* of chronic AR, during which the left ventricle adapts to volume overload via eccentric hypertrophy and dilation to maintain a relatively stable forward stroke volume, keeping peripheral waveform characteristics constant for years. The sharp rise in performance in the proximate group suggests the model acutely captures the hemodynamic instability marking the transition from compensation to decompensation.

This sensitivity to disease progression translates into valuable clinical screening efficacy. As shown in Table 3, even within the “opportunity window” of 1–3 years prior to clinical diagnosis, the model identified 49.1% of AS patients and 44.8% of AR patients while maintaining a specificity of 80%. This implies that PiLA has the capability to screen out nearly half of the high-risk individuals using low-cost means while patients are still in the asymptomatic latent period. Notably, even 10 years before diagnosis, the model’s discriminative ability remains superior to random guessing, suggesting that PPG signals may serve as an ultra-early biomarker, capturing subclinical vascular mechanical changes decades before the onset of macroscopic clinical symptoms.

Long-term Risk Stratification and Independent Prognostic Value

To verify whether the prognostic value of PiLA features is independent of potential confounding factors, we designed a dual-validation strategy comprising multivariable Cox regression in the total cohort and rigorous survival analysis based on Propensity Score Matching (PSM). This combined approach aims to comprehensively evaluate the model’s robustness under different statistical assumptions.

In the multivariable Cox regression analysis of the total cohort, we constructed three progressive adjustment models to quantify the association between PiLA scores and the risk of future aortic valve disease. Model 1 adjusted only for basic demographic characteristics including age, sex, and BMI. Model 2 further incorporated systolic blood pressure, diastolic blood pressure, and smoking status to control for hemodynamic and lifestyle factors. Model 3 additionally adjusted for diabetes, chronic kidney disease, and history of cardiovascular diseases which specifically includes high blood pressure, heart attack, angina, and stroke, constituting the most stringent test for independence.

Table 4: Multivariable Cox Regression Analysis for Incident Aortic Valve Disease in the Total Cohort

Outcome	Model	Adjustments	HR (95% CI)	P-value
Aortic Stenosis (AS)	1	Age, Sex, BMI	1.42 (1.35–1.49)	$< 10^{-47}$
	2	model 1+ SBP, DBP, Smoking	1.37 (1.31–1.44)	$< 10^{-38}$
	3	model 2+ Diabetes, CKD, CVD History	1.33 (1.27–1.39)	$< 10^{-31}$
Aortic Regurgitation (AR)	1	Age, Sex, BMI	1.43 (1.34–1.53)	$< 10^{-27}$
	2	model 1+ SBP, DBP, Smoking	1.41 (1.32–1.50)	$< 10^{-25}$
	3	model 2+ Diabetes, CKD, CVD History	1.38 (1.29–1.47)	$< 10^{-22}$

As shown in Table 4, in Model 1, each standard deviation increase in the AI score was associated with a 41.7% increase in the risk of aortic stenosis (HR 1.417, $p < 10^{-47}$) and a 43.1%

increase in the risk of aortic regurgitation (HR 1.431, $p < 10^{-27}$). Notably, even with the comprehensive clinical covariate adjustments in Model 2 and Model 3, these associations exhibited high stability with only minimal attenuation in hazard ratios. In the fully adjusted Model 3, the hazard ratios for aortic stenosis and regurgitation remained at 1.328 and 1.378, respectively, both retaining high statistical significance. This cross-model consistency indicates that the AI model captures specific pulse waveform morphological features independent of traditional clinical risk factors.

To further validate this finding under more controlled conditions, we conducted a survival analysis experiment based on Propensity Score Matching. We precisely matched each case in the massive cohort with control individuals, strictly controlling for eight key physiological indicators including age, sex, systolic blood pressure, diastolic blood pressure, heart rate, BMI, history of diabetes, and history of cardiovascular disease covering high blood pressure, thereby ensuring a Standardized Mean Difference (SMD) < 0.1 . This design intentionally eliminated inter-group differences in traditional risk factors, forcing the model to rely solely on subtle morphological cues embedded in the PPG waveform for discrimination, thereby constituting an extreme stress test for the model's feature extraction capabilities.

In this highly balanced cohort (AS group $n = 6,786$; AR group $n = 3,527$), Kaplan-Meier event-free survival curves revealed a significant and monotonic dose-response gradient between model-predicted probabilities and long-term incidence risk. Notably, as we employed a landmark analysis design with a one-year observation window to exclude potential subclinical prevalent cases, no events were recorded within the first 365 days of follow-up. Following this landmark period, for aortic stenosis (Figure 4A), the survival trajectories of the four risk quartiles (Q1–Q4) showed clear stepwise separation. Cox proportional hazards regression analysis indicated that individuals classified into the highest risk group (Q4) had a long-term incidence risk 2.31 times that of the lowest risk group (Q1) (95% CI: 1.98–2.70, $p < 0.0001$). This implies that even with perfectly matched baseline physiological characteristics, the unique hemodynamic fingerprints in the PPG waveform can independently identify high-risk individuals. For aortic regurgitation, which involves more complex pathological mechanisms (Figure 4B), the model also demonstrated robust stratification capability, with a Hazard Ratio (HR) of 2.02 for the Q4 group relative to Q1 (95% CI: 1.63–2.50, $p < 0.0001$), confirming the long-term prognostic significance of the model's capture of diastolic regurgitation load.

Further examining the effectiveness of clinical screening strategies, we defined the top 25% of risk scores as "High-Risk Screening Targets." As shown in Figure 4C and D, their survival curves significantly deviated from the remaining 75% low-risk population early in the follow-up period (Log-Rank $p < 0.0001$). Individuals flagged as high-risk by the model had a 68% increased risk of developing aortic stenosis (HR=1.68) and a 63% increased risk for aortic regurgitation (HR=1.63). These results powerfully demonstrate that the deep morphological features extracted by PILA possess strong diagnostic screening value independent of traditional clinical risk factors, filling the screening blind spot between "risk factor exposure" and "clinical symptom manifestation."

Subgroup Analysis and Physiological Heterogeneity

To assess the consistency of model performance across diverse physiological backgrounds and verify whether the model captures genuine hemodynamic features rather than statistical spurious correlations, we conducted a comprehensive stratified validation on the 6,377 subjects included in the study. The forest plots (Figure 5) reveal a critical finding: while the model maintains basic discriminative ability across all subgroups, significant inter-group differences profoundly reflect the complexity of PPG waveform modulation by individual physiological states, aligning closely

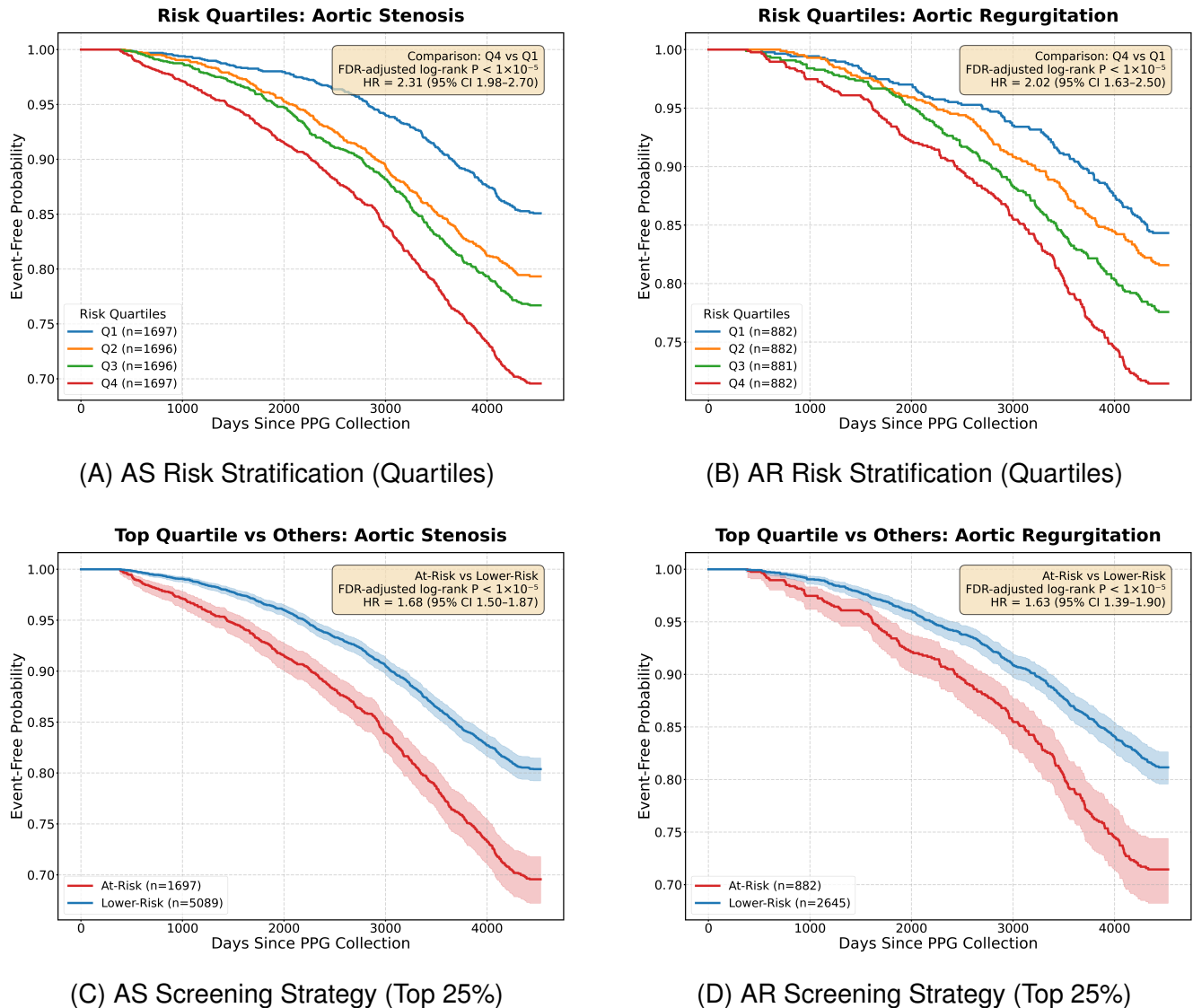


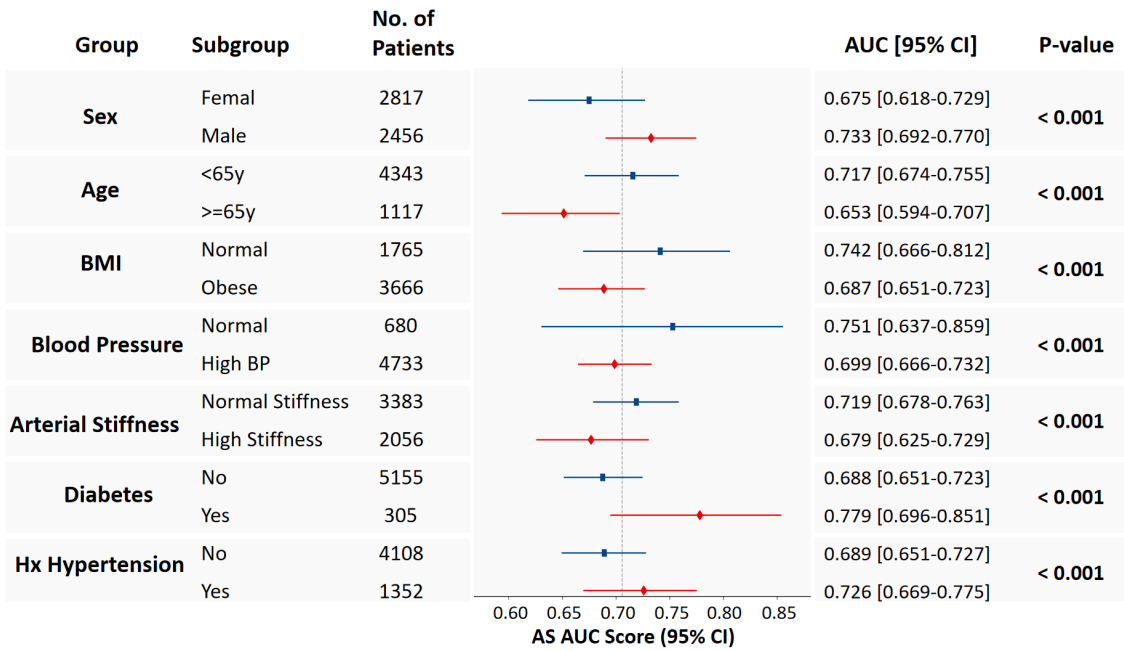
Figure 4: Kaplan-Meier survival analysis in the PSM-matched cohort. **(A, B)** Fine-grained risk stratification by quartiles shows a clear dose-response relationship for both AS and AR. **(C, D)** Evaluation of a binary clinical screening strategy (Top 25% vs. Others) demonstrates significant separation in survival curves, validating the model's utility for early identification of high-risk populations.

with cardiovascular fluid dynamics principles.

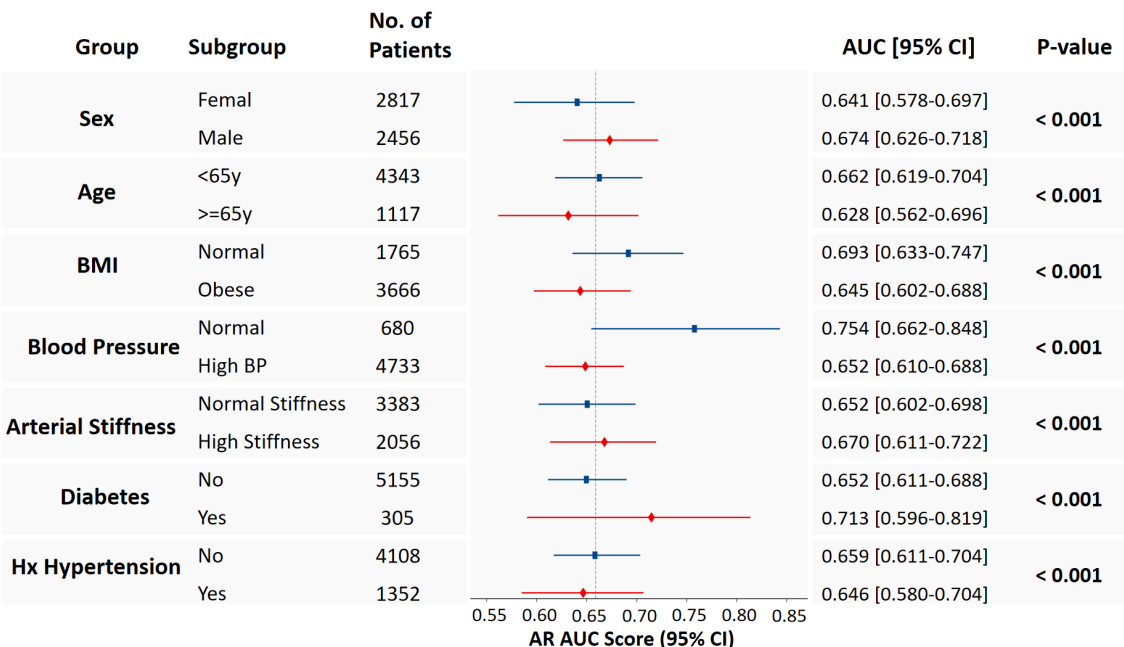
First, vascular aging and stiffening exhibited a significant “Masking Effect” on feature extraction, particularly in the AS detection task. We set the age cutoff at the clinically standard 65 years, and results showed that model performance in the <65 years group (AUC 0.717) was significantly superior to that in the ≥ 65 years group (AUC 0.652, $P < 0.001$). To confirm that this difference stems from physical vascular properties rather than age itself, we introduced the Arterial Stiffness Index (ASI) for validation. The results demonstrated a significant performance gap in AS screening between the normal vascular elasticity group (AUC 0.718) and the high stiffness group (AUC 0.679). This phenomenon has a plausible pathophysiological explanation: our PG-SSL paradigm is pre-trained based on textbook-defined typical AS waveforms (e.g., Pulsus Tardus). In younger individuals or those with better vascular compliance, hemodynamic changes caused by valvular stenosis (such as delayed upstroke) are fully projected onto the peripheral waveform. However, in elderly or high-stiffness populations, the enhanced pulse wave reflection caused by arterial stiffening steepens the waveform upstroke. This physical “pseudo-normalization” partially counteracts and masks the specific fingerprints of AS. Conversely, this proves that the model has indeed learned the fine-grained morphological features associated with AS, rather than simple clinical covariates. A similar trend appeared in the diabetes and obesity subgroups: chronic hyperglycemia and obesity-induced systemic arteriosclerosis and microvascular dysfunction likely weaken pathological features in the peripheral waveform through similar mechanisms, leading to a slight decline in model performance.

Second, hemodynamic load predictably interfered with detection performance, primarily in the AR task. The most significant physiological interaction appeared in the relationship between AR detection and blood pressure. The model’s AUC reached 0.753 in the normotensive group but dropped to 0.650 in the hypertensive group. This aligns with fluid dynamics principles: increased peripheral afterload caused by hypertension restricts diastolic blood regurgitation, thereby weakening the typical “Water-Hammer Pulse” features of AR (i.e., widened pulse pressure and rapid collapse). This implies that in clinical applications, hypertension is a significant confounding factor, suggesting that AR screening should be coupled with blood pressure control or correction. Furthermore, the model demonstrated a degree of sexual dimorphism. Performance in male subjects was generally superior to females, particularly in the AS task. This may relate to sex-specific pathophysiological differences in AS: males tend to develop a more typical phenotype of valvular calcification and left ventricular dilation, resulting in more drastic hemodynamic changes; whereas females often present with small left ventricles, low flow, and more severe myocardial fibrosis, a cryptic phenotype that projects more faintly onto the PPG waveform³⁸.

In summary, the subgroup analysis results honestly map the heterogeneity of physiological signals in the real world. Given the extreme scarcity of positive samples in this study, the model cannot fully cover the waveform variation space of all complex physiological subtypes. Nevertheless, the performance trends exhibited by the model across major physiological dimensions are highly consistent with known cardiovascular mechanical laws—performing best under conditions of good vascular compliance and low interference load. This performance fluctuation, which aligns with physiological expectations, powerfully proves that PILA does not rely on simple statistical spurious correlations but has successfully captured genuine hemodynamic signals essential to valvular pathology, indicating its higher potential diagnostic efficacy under ideal physiological conditions or with appropriate correction.



(a) AS Subgroup Analysis



(b) AR Subgroup Analysis

Figure 5: Forest plots of subgroup analysis for (a) Aortic Stenosis and (b) Aortic Regurgitation. The model shows consistent performance trends across major physiological dimensions.

DISCUSSION

The management of cardiovascular diseases is undergoing a paradigm shift from traditional symptom-driven models towards proactive early screening enabled by wearable technologies^{39,40}. Such opportunistic screening strategies have demonstrated significant potential in improving detection rates of occult conditions while offering substantial cost-effectiveness⁴¹. In this context, our study demonstrates the feasibility of large-scale screening for Aortic Valve Disease (AVD) using unlabeled PPG data through the proposed PiLA framework. Constrained by the scarcity of gold-standard labels, we eschewed purely data-driven brute-force approaches in favor of a novel pathway: physiology-guided self-supervised learning. Our results indicate that PiLA achieves superior performance in screening for both Aortic Stenosis (AS) and Aortic Regurgitation (AR) using only a limited number of labeled samples. This offers a promising solution for low-cost, large-scale early screening of AVD in resource-limited settings.

The success of PiLA underscores the importance of high-quality inductive bias in medical AI. Our comparative experiments reveal that not all knowledge integration is beneficial; attempts based on shallow feature clustering resulted in negative transfer. The effectiveness of PiLA lies in injecting specific priors that are highly aligned with pathological mechanisms, such as the “pulsus tardus” morphology. This precise knowledge guidance acts as a filter, forcing the model to decouple genuine hemodynamic signals from complex background noise. This proves that in small-sample scenarios, appropriate and domain-specific knowledge is key to compensating for data shortages.

From a clinical perspective, this study validates the unique value of PPG as a non-invasive hemodynamic window. By directly carrying mechanical information from peripheral blood vessels, PPG possesses a natural physical advantage in detecting mechanical obstructive diseases like AVD. Survival analysis further reveals that microscopic changes in the PPG waveform often precede macroscopic symptoms. Our model can identify high-risk individuals three years prior to diagnosis, suggesting it has the potential to fill the screening blind spot during the asymptomatic phase and secure a valuable opportunity window for early intervention.

Building on this foundation, our study further establishes the PiLA score as an “Independent Hemodynamic Digital Biomarker” through rigorous statistical adjustment. Under the dual validation of multivariable Cox regression and Propensity Score Matching, the model retained significant risk stratification capability even after isolating the confounding influences of traditional risk factors such as age, hypertension, and BMI. This powerfully demonstrates that the deep learning model functions not merely as a “proxy” for existing clinical covariates, but rather extracts orthogonal pathological fingerprints from the waveform that are invisible to traditional metrics. This independence endows PPG signals with a new dimension beyond routine vital sign monitoring, enabling the provision of incremental information supplementary to current clinical assessment systems. Consequently, it effectively fills the screening “blind spot” between risk factor exposure and the manifestation of macroscopic symptoms.

Despite the large-scale collection of physiological signals via wearable devices, acquiring matched high-quality clinical gold-standard labels remains a significant resource bottleneck. Previous research has highlighted that the expert-level annotation of medical data is not only time-consuming and costly but also constitutes a primary barrier to the clinical generalization of AI models, leading to a “data-rich, label-poor” dilemma⁴². This challenge is particularly pronounced in PPG signal analysis, where significant inter-subject physiological variability makes supervised learning paradigms prone to overfitting in label-scarce scenarios⁴³. Against this backdrop, the research focus in artificial intelligence is undergoing a profound paradigm shift from a model-centric to a data-centric approach, which emphasizes mining the latent value within data itself⁴⁴. The success of PiLA is a strong testament to this shift: by transforming unlabeled data

into knowledge through physiological priors, PiLA effectively extracts robust pathological features from massive, heterogeneous data. Despite these successes, our methodology remains exploratory. The threshold-based generation of pseudo-labels appears somewhat rigid when dealing with individual variability, inevitably introducing label noise. However, experimental results suggest a favorable compatibility between deep learning models and massive datasets: the statistical regularities in large-scale data help the model tolerate and correct for this rule-based noise, enabling it to learn robust features that transcend the rules themselves. In summary, this study not only confirms the unique value of PPG as a direct and accessible hemodynamic surrogate but, more importantly, validates that domain-knowledge-driven self-supervision is a viable pathway to navigate the data scarcity dilemma in medical AI. By encoding clinical pathological priors into self-supervised proxy tasks, this work lays a solid foundation for establishing a low-cost, ubiquitous AVD screening system. We anticipate that these findings will accelerate the clinical translation of wearable technologies for structural heart disease management, ultimately improving cardiovascular health outcomes on a global scale.

RESOURCE AVAILABILITY

Lead Contact

Further information and requests for resources should be directed to and will be fulfilled by the lead contact, Shenda Hong (hongshenda@pku.edu.cn).

Materials Availability

This study did not generate new unique reagents.

Data and Code Availability

- **Data:** The individual-level physiological data used in this study are sourced from the UK Biobank and are not publicly available due to patient privacy restrictions and data usage agreements. Researchers interested in accessing the data must apply directly to the UK Biobank at <https://www.ukbiobank.ac.uk>. The UK Biobank received ethical approval from the National Information Governance Board for Health and Social Care and the National Health Service North West Centre for Research Ethics Committee (Ref: 21/NW/0157).
- **Code:** All original code for the PiLA framework has been deposited at <https://github.com/EZAIJ/PiLA-PPG> and <https://github.com/PKUDigitalHealth/PiLA-PPG> are publicly available as of the date of publication.
- **Additional Info:** Any further inquiries regarding the *implementation details or model architecture* are available from the lead contact upon request.

METHODS

Formal Problem Definition

The primary challenge addressed in this research is the robust screening of Aortic Valve Disease (AVD) from Photoplethysmography (PPG) signals under the realistic constraint of extreme scarcity in gold-standard clinical labels.

To tackle this, we formalize the problem as a *Physiology-Guided Self-Supervised Transfer Learning Task*.

Specifically, we consider two distinct types of datasets:

- A *large-scale dataset without specific pathological labels*, denoted as $\mathcal{D}_U = \{\mathbf{x}_i\}_{i=1}^{N_U}$. Each sample $\mathbf{x}_i \in \mathbb{R}^L$ is a pre-processed PPG time-series segment of length L . Crucially, this dataset is augmented with physiological metadata derived from pulse wave analysis, which enables the generation of proxy labels for our self-supervised pretext task.
- A *small-scale target dataset with gold-standard AVD labels*, denoted as $\mathcal{D}_L = \{(\mathbf{x}_j, \mathbf{y}_j)\}_{j=1}^{N_L}$, where the number of samples is significantly smaller than in the unlabeled set ($N_L \ll N_U$). The label for each sample is a binary vector $\mathbf{y}_j = [y_j^{(\text{AS})}, y_j^{(\text{AR})}] \in \{0, 1\}^2$, indicating the presence or absence of Aortic Stenosis (AS) and Aortic Regurgitation (AR), respectively, as confirmed by echocardiography.

Our central objective is to learn a powerful deep learning model $F : \mathbb{R}^L \rightarrow [0, 1]^2$, which is composed of a feature encoder $f_\theta(\cdot)$ and a classifier $g_\phi(\cdot)$, such that $F(\cdot) = g_\phi(f_\theta(\cdot))$.

The encoder f_θ , parameterized by θ , is primarily pre-trained on the large-scale dataset \mathcal{D}_U through a bespoke physiology-guided self-supervised proxy task. This pre-training stage aims to distill a universal feature representation that is highly sensitive to complex cardiovascular dynamics.

Subsequently, the entire model is efficiently fine-tuned on the small labeled dataset \mathcal{D}_L to achieve accurate and reliable screening for both AS and AR.

Overall Architecture

To address the challenge of AVD screening in a label-scarce environment, we propose an innovative framework named the **Physiology-informed Learning Architecture** (PiLA). Serving as the concrete implementation of the PG-SSL paradigm, the core of this framework lies in the synergistic interplay of two key innovative modules:

1. **PPG Morphological Phenotyping for AVD:** An analysis module responsible for systematically identifying and quantifying abnormal PPG patterns associated with the pathological states of aortic stenosis and regurgitation from a physiological perspective.
2. **Physiology-Guided Self-Supervised Learning (PG-SSL):** An advanced deep learning framework that leverages the physiological patterns defined by the first module as prior knowledge. It addresses the model learning problem through a pipeline of self-supervised pre-training and subsequent gated knowledge-fusion fine-tuning.

Our overall workflow, as illustrated in Figure 6, clearly demonstrates how these two modules collaborate within a three-stage process encompassing data collection, pre-training, and fine-tuning. This integrated process enables end-to-end prediction of AVD from raw PPG signals.

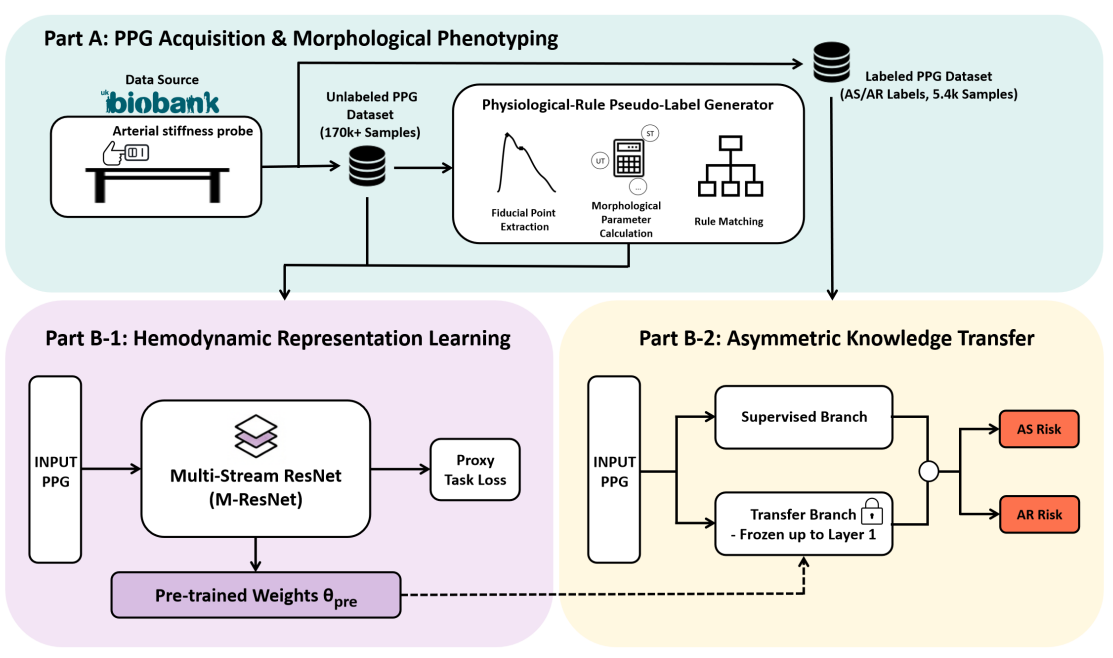


Figure 6: The overall architecture of the PiLA framework. The workflow illustrates the process from acquiring PPG signals from the UK Biobank and constructing a pseudo-label dataset via a physiological rule generator (Part A), to hemodynamic representation learning using M-ResNet (Part B-1), and finally to asymmetric knowledge transfer for AS and AR risk prediction (Part B-2).

PPG Morphological Phenotyping for AVD

This module aims to establish a solid physiological foundation for our machine learning framework. Its core task is to systematically identify and quantify a series of abnormal PPG patterns that are directly associated with the pathological states of Aortic Valve Disease (AVD). By translating complex clinical physiological knowledge into a set of computable PPG-derived digital biomarkers, this module provides high-quality, physiologically interpretable prior knowledge for the subsequent self-supervised learning phase.

Hemodynamic Principles of AVD on Pulse Waveforms

Aortic stenosis (AS) and aortic regurgitation (AR) leave characteristic imprints on the arterial pulse wave through distinct hemodynamic mechanisms. These morphological changes, originating from the central arterial pressure wave, can be non-invasively captured by peripheral PPG signals¹².

In AS, the calcified aortic valve restricts outflow, leading to a significant increase in left ventricular ejection impedance. The blood flow is forced through a narrowed orifice, which not only prolongs the ejection time but also, due to the sustained pressure gradient, creates a characteristic pulse with a slow-rising upstroke and a delayed peak, known as *pulsus tardus*⁴⁵. In severe AS, a secondary shock wave at the stenotic valve can also cause a distinct notch on the upstroke, forming an *anacrotic pulse*.

In AR, the incomplete closure of the aortic valve allows blood to regurgitate back into the left ventricle during diastole. This compels the heart to eject an augmented stroke volume under a hyperdynamic state during systole. The rapid ejection of a large volume of blood against a low-resistance periphery creates a steep upstroke, while the diastolic pressure plummets due to the backflow. Together, these effects result in a widened pulse pressure and a rapidly rising and falling pulse known as the *water-hammer pulse* (WHP)⁴⁶. From a hemodynamic perspective,

these abnormal patterns precisely capture the core pathophysiological features of AS and AR across the dimensions of ejection timing, velocity, and flow impact morphology.

Quantification Framework for PPG Digital Biomarkers

Although the aforementioned pathological patterns are theoretically distinct, their reliable identification in real-world peripheral PPG signals is complicated by a multitude of confounding physiological factors. A key confounder is arterial stiffness, which increases with age. Increased stiffness accelerates the return of the reflected pulse wave, causing it to superimpose on the systolic phase, which can lead to a forward shift of the peak and alterations in the dicrotic notch morphology¹⁴. Some of these age-related physiological changes can mimic the features of AR, leading to significant confusion. Furthermore, the PPG waveform is dynamically modulated by other physiological states, such as heart rate and blood pressure, meaning that any heuristic rules based on fixed thresholds will inevitably be noisy and uncertain.

Given this inherent ambiguity and dynamism, we propose a framework for quantifying these biomarkers. Our framework is inspired by the methodology of Meghraoui et al.³². The core idea is not to use this rule-set as a perfect classifier, but rather to leverage it to construct a structured pretext task for self-supervised learning. On such a massive dataset, a deep neural network, in its effort to minimize the global loss, must learn beyond simply fitting ambiguous boundary cases. Instead, it is compelled to learn the underlying morphological features that explain the differences among the vast majority of "typical" samples. The scale of the data endows the proxy task with strong statistical robustness, forcing the model to learn stable morphological invariants that are independent of short-term physiological fluctuations.

To achieve this, we draw upon clinical literature to define the pathological patterns and quantify them using pulse wave analysis parameters available in the UK Biobank dataset.

- **Anacrotic Pulse:** Identified by the presence of an algorithmically detected notch (shoulder) on the systolic upstroke of the pulse wave⁴⁷.
- **Pulsus Tardus:** As a hallmark of AS, its definition is grounded in the work of Yoshioka et al.⁴⁸, who identified an upstroke time (UT) greater than 0.156 seconds as a strong indicator of severe AS. To enhance the specificity of our rule, we adopted a stricter criterion, defining this pattern as cases where the ratio of UT to the total systolic time (ST) exceeds 60%.
- **Water-Hammer Pulse (WHP):** This is a classic sign of AR. Research by Boiteau et al.⁴⁹ demonstrated that the UT-to-ST ratio is typically low in AR patients, potentially below 34%. Similarly, to improve the rule's specificity, we set our threshold by defining this pattern as cases where the UT-to-ST ratio is less than 30%.

The outputs of these rules—*Anacrotic*, *Tardus*, *WHP*, and *Normal* (for samples not fitting any of the abnormal patterns)—serve as the four pseudo-labels for our proxy classification task.

The Physiology-Guided Self-Supervised Learning (PG-SSL) Framework

To leverage large-scale unlabeled data for mining latent pathological features under the constraint of clinical label scarcity, and to generalize these features to downstream classification tasks, we propose the PG-SSL framework. As illustrated in Figure 7, this framework comprises two core stages: self-supervised pre-training based on multi-stream enhancement, and fine-tuning based on asymmetric feature complementation.

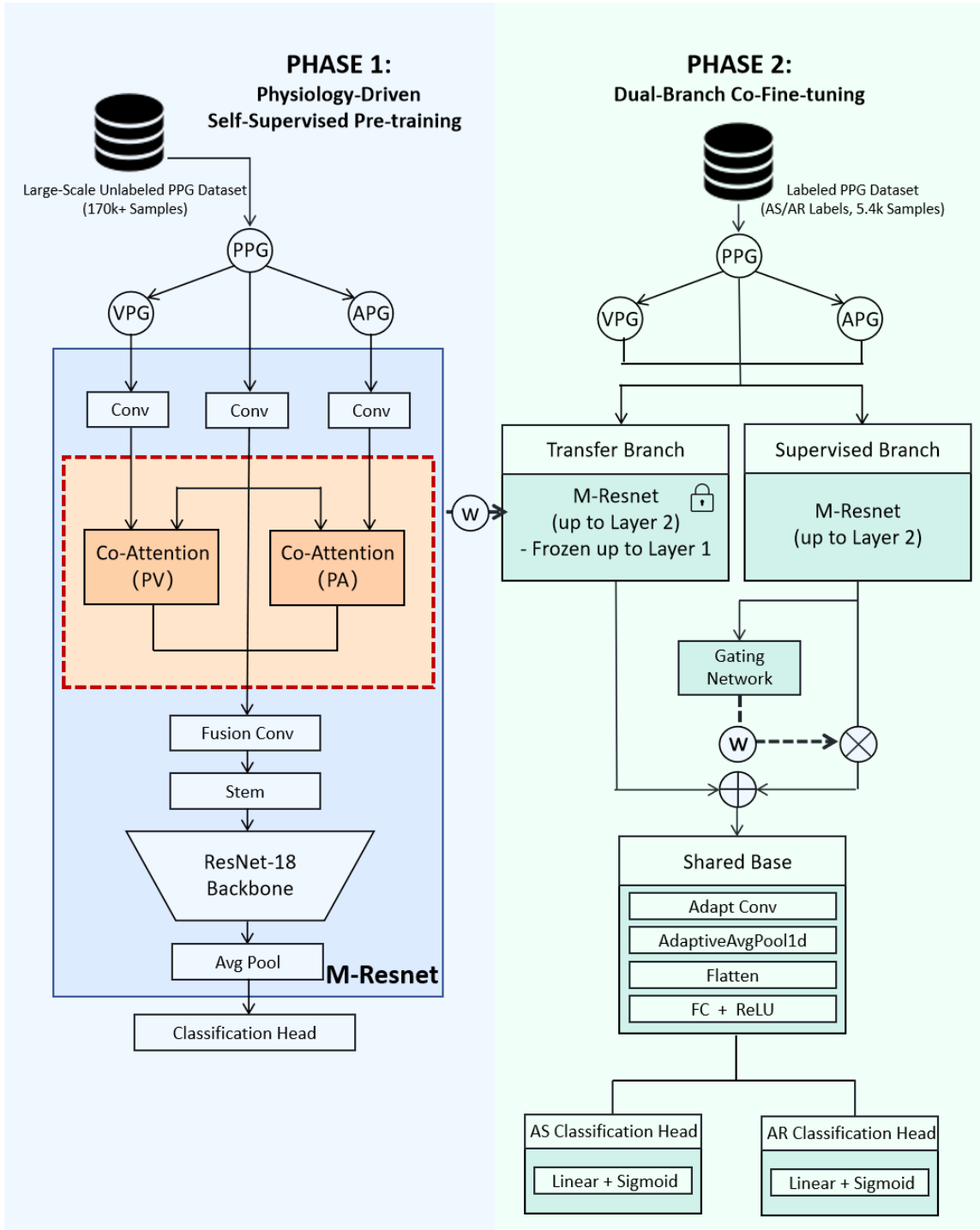


Figure 7: Detailed architecture of the deep learning model. **Phase 1** (Left) depicts the physiology-driven self-supervised pre-training, where M-ResNet takes multi-modal inputs (PPG/VPG/APG) with co-attention mechanisms. **Phase 2** (Right) illustrates the dual-branch co-fine-tuning architecture. The transfer branch loads and partially freezes pre-trained weights, while the supervised branch is trained from scratch. A gating network modulates feature fusion before the shared base for classification.

Pre-training via Pulse Pattern Recognition Task

The first stage aims to extract general hemodynamic features from the large-scale unlabeled dataset \mathcal{D}_U . We utilize the four PPG morphological phenotypes defined in the previous section as pseudo-labels to construct an *Arterial Pulse Pattern Recognition (APPR)* proxy task, forcing the model to distill morphological invariants that are independent of individual differences from massive data.

In terms of architecture design, we construct a feature encoder named Multi-Stream ResNet (M-ResNet). Although the ResNet1D-18 has been widely validated, standard convolutional networks tend to smooth out high-frequency details during downsampling, whereas the core pathological features of AS and AR often manifest as subtle deformations occurring in extremely short instants. To overcome this limitation, we modified the front-end input stem of the ResNet by designing a *multi-modal co-input module*. Specifically, in addition to the raw PPG signal, we explicitly introduce its first derivative (VPG) and second derivative (APG) as parallel input channels. This design leverages the high sensitivity of derivative signals to waveform inflection points, forcing the encoder to establish a phase-locked association between the raw waveform and instantaneous velocity and acceleration at the initial stage of feature extraction. Upon completion of training, we save the optimal weights θ_{pre} as the initialization for subsequent tasks.

Fine-tuning with Asymmetric Feature Complementation

The second stage migrates the pre-trained model to the downstream AS and AR detection tasks. Given the scarcity of clinical labels in \mathcal{D}_L , we design a *dual-branch asymmetric fusion* architecture. This architecture contains two parallel branches, both utilizing the M-ResNet structure described above. To measure mid-level morphological details crucial for diagnosis, we choose to perform feature integration at the intermediate layer (specifically after Layer 2) of the network rather than at the end.

To coordinate generality with specificity, we propose an asymmetric feature complementation strategy. Specifically, we freeze the front-end multi-modal module of the Transfer Branch to lock the underlying physical morphological features, while transmitting its output feature h_{ssl} directly as a foundational representation. In contrast, the Supervised Branch is initialized from scratch to capture the distribution characteristics of the specific dataset, denoted as h_{task} . To prevent this branch from introducing random noise due to the small data volume, we introduce a lightweight gating network as a “correlation filter” to dynamically suppress low-confidence features. Finally, the fused feature is obtained via the formula $h_{fused} = h_{ssl} + (h_{task} \odot w_{gate})$. This mechanism ensures that the model retains the complete general representation while only adding filtered, high-value task-specific cues as an increment.

Finally, the fused features are sent into a shared backend network for deep integration and are used to predict the probabilities of AS and AR respectively through two independent linear classification heads. The entire model is optimized end-to-end during the fine-tuning phase using a Weighted Binary Cross-Entropy Loss to mitigate the impact of positive-negative sample imbalance.

ACKNOWLEDGMENTS

This work was supported in part by the National Natural Science Foundation of China under Grant 62102008, Grant 62202332, Grant 62376197, Grant 62020106004 and Grant 92048301; in part by the CCF-Zhipu Large Model Innovation Fund (CCF-Zhipu202414); in part by the CCF-Tencent Rhino-Bird Open Research Fund (CCF-Tencent RAGR20250108); in part by the Tian-

jin Science and Technology Program under Grant 23JCYBJC00360; in part by the Research Project of Peking University in the State Key Laboratory of Vascular Homeostasis and Remodeling (2025-SKLVHR-YCTS-02); in part by the PKU-OPPO Fund (BO202301, BO202503).

DECLARATION OF INTERESTS

The authors declare no competing interests.

References

1. Coffey, S., Roberts-Thomson, R., Brown, A., Carapetis, J., Chen, M., Enriquez-Sarano, M., Zühlke, L., and Prendergast, B.D. (2021). Global epidemiology of valvular heart disease. *Nature Reviews Cardiology* *18*, 853–864. doi: [10.1038/s41569-021-00570-z](https://doi.org/10.1038/s41569-021-00570-z).
2. Aluru, J.S., Barsouk, A., Saginala, K., Rawla, P., and Barsouk, A. (2022). Valvular heart disease epidemiology. *Medical Sciences* *10*, 32. doi: [10.3390/medsci10020032](https://doi.org/10.3390/medsci10020032).
3. Thoenes, M., Bramlage, P., Zamorano, P., Messika-Zeitoun, D., Wendt, D., Kasel, M., Kuruucova, J., and Steeds, R.P. (2018). Patient screening for early detection of aortic stenosis (as)—review of current practice and future perspectives. *Journal of Thoracic Disease* *10*, 5584–5594. doi: [10.21037/jtd.2018.09.02](https://doi.org/10.21037/jtd.2018.09.02).
4. ESC/EACTS Task Force (2025). 2025 esc/eacts guidelines for the management of valvular heart disease. *European Heart Journal*. doi: [10.1093/eurheartj/ehaf194](https://doi.org/10.1093/eurheartj/ehaf194).
5. Khade, P.J., Mane, P., Mahore, S., and Bhole, K. (2021). Machine learning approach for prediction of aortic and mitral regurgitation based on phonocardiogram signal. In 2021 12th International Conference on Computing Communication and Networking Technologies (ICCCNT) (IEEE, 2021).. doi: [10.1109/ICCCNT51525.2021.9579971](https://doi.org/10.1109/ICCCNT51525.2021.9579971).
6. Erin, E., and Semiz, B. (2024). Performance comparison of gyrocardiogram and seismo-cardiogram signals in valvular heart disease assessment. In BIOSTEC 2024: Proceedings of the 17th International Joint Conference on Biomedical Engineering Systems and Technologies (SCITEPRESS, 2024).. doi: [10.5220/0012441700003657](https://doi.org/10.5220/0012441700003657).
7. Saraf, K., Baek, C.I., Wasko, M.H., Zhang, X., Zheng, Y., Borgstrom, P.H., Mahajan, A., and Kaiser, W.J. (2019). Fully-automated diagnosis of aortic stenosis using phonocardiogram-based features. In 2019 41st Annual International Conference of the IEEE Engineering in Medicine and Biology Society (EMBC) (IEEE, 2019).. doi: [10.1109/EMBC.2019.8857506](https://doi.org/10.1109/EMBC.2019.8857506).
8. Cohen-Shelly, M., Attia, Z.I., Friedman, P.A., Ito, S., Essayagh, B.A., Ko, W.Y., Murphree, D.H., Michelena, H.I., Enriquez-Sarano, M., and Carter, R.E. (2021). Electrocardiogram screening for aortic valve stenosis using artificial intelligence. *European Heart Journal* *42*, 2885–2896. doi: [10.1093/eurheartj/ehab153](https://doi.org/10.1093/eurheartj/ehab153).
9. Sawano, S., Kodera, S., Katsushika, S., Nakamoto, M., Ninomiya, K., Shinohara, H., Higashikuni, Y., Nakanishi, K., Nakao, T., and Seki, T. (2022). Deep learning model to detect significant aortic regurgitation using electrocardiography. *Journal of Cardiology* *79*, 334–341. doi: [10.1016/j.jjcc.2021.08.029](https://doi.org/10.1016/j.jjcc.2021.08.029).

10. Pereira, T., Tran, N., Gadhouni, K., Pelter, M.M., Do, D.H., Lee, R.J., Colorado, R., Meisel, K., and Hu, X. (2020). Photoplethysmography based atrial fibrillation detection: a review. *npj Digital Medicine* 3, 3. doi: 10.1038/s41746-019-0207-9.
11. Allen, J. (2007). Photoplethysmography and its application in clinical physiological measurement. *Physiological Measurement* 28, R1–R39. doi: 10.1088/0967-3334/28/3/R01.
12. Millasseau, S.C., Ritter, J.M., Takazawa, K., and Chowienczyk, P.J. (2006). Contour analysis of the photoplethysmographic pulse measured at the finger. *Journal of Hypertension* 24, 1449–1456. doi: 10.1097/01.hjh.0000239277.05068.87.
13. Elgendi, M., Fletcher, R., Liang, Y., Howard, N., Lovell, N.H., Abbott, D., Lim, K., and Ward, R. (2019). The use of photoplethysmography for assessing hypertension. *npj Digital Medicine* 2, 60. doi: 10.1038/s41746-019-0136-7.
14. Karimpour, P., May, J.M., and Kyriacou, P.A. (2023). Photoplethysmography for the assessment of arterial stiffness. *Sensors* 23, 9882. doi: 10.3390/s23249882.
15. Yang, R., Kang, L., Zhou, A., Cui, H., and Ma, H. (2024). Aortic stenosis detection by improved inception convolution network-enabled pulse wave. In 2024 IEEE 30th International Conference on Parallel and Distributed Systems (ICPADS) (IEEE, 2024). . doi: 10.1109/ICPADS63350.2024.00024.
16. Kang, L., Yang, R., Liu, Y., Zhou, A., Ma, H., and Cui, H. (2025). PASS: A novel PPG-based aortic stenosis screening system. *Proceedings of the ACM on Interactive, Mobile, Wearable and Ubiquitous Technologies* 9, 1–25. doi: 10.1145/3749548.
17. Krishnan, R., Rajpurkar, P., and Topol, E.J. (2022). Self-supervised learning in medicine and healthcare. *Nature Biomedical Engineering* 6, 1346–1352. doi: 10.1038/s41551-022-00914-1.
18. Zhang, K., Wen, Q., Zhang, C., Cai, R., Jin, M., Liu, Y., Zhang, J.Y., Liang, Y., Pang, G., and Song, D. (2024). Self-supervised learning for time series analysis: Taxonomy, progress, and prospects. *IEEE Transactions on Pattern Analysis and Machine Intelligence* 46, 6775–6794. doi: 10.1109/TPAMI.2024.3387317.
19. McGee, S. (2021). Evidence-Based Physical Diagnosis. 5 ed.. Elsevier.
20. Wu, H., Hu, T., Liu, Y., Zhou, H., Wang, J., and Long, M. (2022). Timesnet: Temporal 2d-variation modeling for general time series analysis. *arXiv preprint arXiv:2210.02186*.
21. Choi, J., Hwang, G., Lee, J.S., Ryu, M., and Lee, S.J. (2023). Weighted knowledge distillation of attention-lrcn for recognizing affective states from ppg signals. *Expert Systems with Applications* 233, 120883. doi: 10.1016/j.eswa.2023.120883.
22. Ding, C., and Wu, C. (2024). Self-supervised learning for biomedical signal processing: A systematic review on ECG and PPG signals. *medRxiv*. . doi: 10.1101/2024.09.30.24314588.
23. Weng, W., Gu, Y., Guo, S., Ma, Y., Yang, Z., Liu, Y., and Chen, Y. (2025). Self-supervised learning for electroencephalogram: A systematic survey. *ACM Computing Surveys* 57, 1–38. doi: 10.1145/3736574.
24. Liu, Z., Alavi, A., Li, M., and Zhang, X. (2023). Self-supervised contrastive learning for medical time series: A systematic review. *Sensors* 23, 4221. doi: 10.3390/s23094221.

25. Banville, H., Chehab, O., Hyvärinen, A., Engemann, D.A., and Gramfort, A. (2021). Uncovering the structure of clinical EEG signals with self-supervised learning. *Journal of Neural Engineering* 18, 046020. doi: 10.1088/1741-2552/abca18.

26. Mehari, T., and Strodthoff, N. (2022). Self-supervised representation learning from 12-lead ECG data. *Computers in Biology and Medicine* 141, 105114. doi: 10.1016/j.combiomed.2021.105114.

27. von Rueden, L., Mayer, S., Beckh, K., Georgiev, B., Giesselbach, S., Heese, R., Kirsch, B., Pfrommer, J., Pick, A., Ramamurthy, R., Walczak, M., Garcke, J., Bauckhage, C., and Schuecker, J. (2023). Informed machine learning: A taxonomy and survey of integrating prior knowledge into learning systems. *IEEE Transactions on Knowledge and Data Engineering* 35, 614–633. doi: 10.1109/TKDE.2021.3079836.

28. Karniadakis, G.E., Kevrekidis, I.G., Lu, L., Perdikaris, P., Wang, S., and Yang, L. (2021). Physics-informed machine learning. *Nature Reviews Physics* 3, 422–440. doi: 10.1038/s42254-021-00314-5.

29. Liu, R., Shen, J., Gu, Y., Chen, Y., Zhang, J., Wu, Q., Xu, C., and Fan, F. (2025). Physcl: Knowledge-aware contrastive learning of physiological signal models for cuff-less blood pressure estimation. *IEEE Journal of Biomedical and Health Informatics* 29, 4728–4740. doi: 10.1109/JBHI.2025.3554495.

30. Maghsoudi, N., Nassar, S., Wilson, P.F.R., To, M.N.N., Mannina, S., Addas, S., Sibley, S., Maslove, D., Abolmaesumi, P., and Mousavi, P. (2025). Domain knowledge is power: Leveraging physiological priors for self-supervised representation learning in electrocardiography.

31. Lee, B.T., Kong, S.T., Song, Y., and Lee, Y. (2021). Self-supervised learning with electrocardiogram delineation for arrhythmia detection. In 2021 43rd Annual International Conference of the IEEE Engineering in Medicine and Biology Society (EMBC) (IEEE, 2021). doi: 10.1109/EMBC46164.2021.9630364.

32. Meghraoui, M.H., Benaired, N., Benselama, Z.A., Yssaad, B., and Benselama, S.I. (2024). Classifying abnormal arterial pulse patterns in cardiovascular diseases: A photoplethysmography and machine learning approach. *Traitement du Signal* 41, 543–562. doi: 10.18280/ts.410210.

33. Abbas, A.E., and Pibarot, P. (2019). Hemodynamic characterization of aortic stenosis states. *Catheterization and Cardiovascular Interventions* 93, 1002–1023. doi: 10.1002/ccd.28146.

34. Hungerford, S.L., Adji, A.I., and Kapur, N.K. (2023). Interpretation of the central aortic pressure waveform in elderly patients with aortic stenosis. *American Journal of Physiology - Heart and Circulatory Physiology* 324, H697–H712. doi: 10.1152/ajpheart.00050.2023.

35. Piccioli, F., Li, Y., Valiani, A., Caleffi, V., Chowienczyk, P., and Alastrauey, J. (2023). Cardiac contractility is a key factor in determining pulse pressure and its peripheral amplification. *Frontiers in Cardiovascular Medicine* 10, 1197842. doi: 10.3389/fcvm.2023.1197842.

36. Yu, S., and McEnery, C.M. (2020). Central versus peripheral artery stiffening and cardiovascular risk. *Arteriosclerosis, Thrombosis, and Vascular Biology* 40, 1028–1033. doi: 10.1161/ATVBAHA.120.313128.

37. Elgendi, M. (2012). On the analysis of fingertip photoplethysmogram signals. *Current Cardiology Reviews* 8, 14–25. doi: 10.2174/157340312801215782.

38. Saeed, S., Dweck, M.R., and Chambers, J. (2020). Sex differences in aortic stenosis: from pathophysiology to treatment. *Expert Review of Cardiovascular Therapy* 18, 65–76. doi: 10.1080/14779072.2020.1732209.

39. Pedroso, A.F., and Khera, R. (2025). Leveraging ai-enhanced digital health with consumer devices for scalable cardiovascular screening, prediction, and monitoring. *npj Cardiovascular Health* 2, 34. doi: 10.1038/s44325-025-00071-9.

40. Wong, K.C., Nguyen, T.N., and Chow, C.K. (2024). Global implementation and evaluation of atrial fibrillation screening in the past two decades—a narrative review. *npj Cardiovascular Health* 1, 17. doi: 10.1038/s44325-024-00014-w.

41. Chen, W., Khurshid, S., Singer, D.E., Atlas, S.J., Ashburner, J.M., Ellinor, P.T., McManus, D.D., Lubitz, S.A., and Chhatwal, J. (2022). Cost-effectiveness of screening for atrial fibrillation using wearable devices. *JAMA Health Forum* 3, e222419. doi: 10.1001/jamahealthforum.2022.2419.

42. Azizi, S., Culp, L., Freyberg, J., Mustafa, B., Baur, S., Kornblith, S., Chen, T., Tomasev, N., Mitrović, J., Strachan, P., Mahdavi, S.S., Wulczyn, E., Babenko, B., Walker, M., Loh, A., Chen, P.H.C., Liu, Y., Bavishi, P., McKinney, S.M., Winkens, J., Guha Roy, A., Beaver, Z., Ryan, F., Krogue, J.D., Etemadi, M., Telang, U., Liu, Y., Peng, L., Corrado, G.S., Webster, D.R., Fleet, D., Hinton, G., Houlsby, N., Karthikesalingam, A., Norouzi, M., and Natarajan, V. (2023). Robust and data-efficient generalization of self-supervised machine learning for diagnostic imaging. *Nature Biomedical Engineering* 7, 756–779. doi: 10.1038/s41551-023-01049-7.

43. Ghorbani, R., Reinders, M.J.T., and Tax, D.M.J. (2023). Self-supervised ppg representation learning shows high inter-subject variability. In Proceedings of the 8th International Conference on Machine Learning Technologies (ICMLT) (2023)..

44. Majeed, A., and Hwang, S.O. (2024). A data-centric ai paradigm for socio-industrial and global challenges. *Electronics* 13, 2156. doi: 10.3390/electronics13112156.

45. Moxham, I.M. (2003). Understanding arterial pressure waveforms. *Southern African Journal of Anaesthesia and Analgesia* 9, 40–42. doi: 10.1080/22201173.2003.10872991.

46. Suvarna, J. (2008). Watson's water hammer pulse. *Journal of Postgraduate Medicine* 54, 163.

47. Fleming, P.R. (1957). The mechanism of the pulsus bisferiens. *British Heart Journal* 19, 519–524.

48. Yoshioka, N., Fujita, Y., Yasukawa, T., Sano, I., Kiso, M., Nakayama, M., and Yoshida, Y. (2010). Do radial arterial pressure curves have diagnostic validity for identify severe aortic stenosis? *Journal of Anesthesia* 24, 7–10. doi: 10.1007/s00540-009-0837-1.

49. Boiteau, G.M., Libanoff, A.J., and Allenstein, B.J. (1964). Upstroke time ratio in valvular aortic insufficiency. *The American Journal of Cardiology* 14, 162–168. doi: 10.1016/0002-9149(64)90127-4.

APPENDIX

Definition of Handcrafted PPG Features

Table S5 lists the 22 handcrafted PPG morphological features used in the late fusion experiment. These features were extracted to cover temporal, slope, and statistical characteristics of the waveform.

Table S5: Definitions of 22 Handcrafted PPG Morphological Features

Symbol	Description
<i>Time Intervals</i>	
T_1	Time from onset to systolic peak
T_2	Time from systolic peak to dicrotic notch
T_3	Time from dicrotic notch to end of cycle
T_4	Time from onset to dicrotic notch
T_5	Time from systolic peak to end of cycle
<i>Waveform Slopes</i>	
$Slope_1$	Slope from onset to systolic peak
$Slope_2$	Slope from onset to dicrotic notch
$Slope_3$	Slope between systolic peak and dicrotic notch
$Slope_4$	Slope between dicrotic notch and end of cycle
$Slope_5$	Slope between systolic peak and end of cycle
<i>Mean Values</i>	
$M_1 - M_6$	Mean values of waveform segments defined by $T_1 - T_5$ and total duration
<i>Kurtosis</i>	
$KR_1 - KR_6$	Kurtosis of waveform segments defined by $T_1 - T_5$ and total duration

Baseline Balance Assessment after Propensity Score Matching

To ensure the validity of the comparative survival analysis, we assessed the covariate balance between the case and control groups after Propensity Score Matching (PSM). Table S6 presents the Standardized Mean Differences (SMD) for all eight matched covariates in both the Aortic Stenosis (AS) and Aortic Regurgitation (AR) cohorts. An absolute SMD value of less than 0.1 is considered to indicate a negligible difference between groups, confirming that the baseline physiological characteristics were well-balanced.

Table S6: Covariate Balance Assessment (SMD) in the Matched Cohorts

Covariate	AS Cohort	AR Cohort
	SMD	SMD
Age	0.033	0.051
Sex	0.005	0.008
Systolic Blood Pressure	0.020	0.076
Diastolic Blood Pressure	0.034	0.063
Heart Rate (Pulse)	0.052	0.050
Body Mass Index (BMI)	0.091	0.063
Diabetes History	0.045	0.059
CVD History	0.007	0.016

Note: SMD: Standardized Mean Difference. All SMD values are absolute and below the threshold of 0.1, indicating successful matching and balanced baseline characteristics.